MNRAS **000**, 1–13 (2022) Preprint 19 December 2022 Compiled using MNRAS LATEX style file v3.0

Steady states of the Parker instability: the effects of rotation

Devika Tharakkal[1], Anvar Shukurov[1], Frederick A. Gent[2,1], Graeme R. Sarson[1], Andrew Snodin[3,1]
[1] *School of Mathematics, Statistics and Physics, Newcastle University, Newcastle upon Tyne, NE1 7RU, UK*
[2] *Astroinformatics, Department of Computer Science, Aalto University, PO Box 15400, FI-00076 Espoo, Finland*
[3] *UKAEA, Culham Science Centre, Abingdon, OX14 3DB, UK*

Accepted XXX. Received YYY; in original form ZZZ

ABSTRACT

We model the Parker instability in vertically stratified isothermal gas using non-ideal MHD three-dimensional simulations. Rotation, especially differential, more strongly and diversely affects the nonlinear state than the linear stage (where we confirm the most important conclusions of analytical models), and stronger than any linear analyses predict. Steady state magnetic fields are stronger and cosmic ray energy density higher than in comparable nonrotating systems. Transient gas outflows induced by the nonlinear instability persist longer, of order 2 Gyr, with rotation. Stratification combined with (differential) rotation drives helical flows, leading to mean-field dynamo. Consequently, the nonlinear state becomes oscillatory (while both the linear instability and the dynamo are non-oscillatory). The horizontal magnetic field near the midplane reverses its direction propagating to higher altitudes as the reversed field spreads buoyantly. The spatial pattern of the large-scale magnetic field may explain the alternating magnetic field directions in the halo of the edge-on galaxy NGC 4631. Our model is unique in producing a large-scale magnetic structure similar to such observation. Furthermore, our simulations show that the mean kinetic helicity of the magnetically driven flows has the sign opposite to that in the conventional non-magnetic flows. This has profound consequences for the nature of the dynamo action and large-scale magnetic field structure in the coronae of spiral galaxies which remain to be systematically explored and understood. We show that the energy density of cosmic rays and magnetic field strength are not correlated at scales of order a kiloparsec.

Key words: instabilities – magnetic fields – MHD – cosmic rays – ISM: structure – galaxies: magnetic fields

1 INTRODUCTION

The Parker instability is a magnetic Rayleigh–Taylor or magnetic buoyancy instability modified by cosmic rays that carry negligible weight but exert significant pressure. The instability is an important element of the large-scale dynamics of the interstellar medium (ISM) as it affects the vertical distributions of the gas, magnetic fields and cosmic rays and can drive gas outflows, thereby affecting the star formation. In our previous work (Tharakkal et al. 2022a), we explored the development of the instability, with a focus on its nonlinear saturation, in a non-rotating disc with imposed unstable distributions of the gas, magnetic field and cosmic rays. Among the essentially nonlinear features of the instability are a transient gas outflow in the weakly nonlinear stage and a strong redistribution of magnetic fields, cosmic rays and thermal gas, resulting in a thinner thermal gas disc and very large scale heights and low energy densities of the magnetic field and cosmic rays. In this paper, we address the effect of rotation on the Parker instability.

Rotation is known to reduce the growth rate of the weak perturbations but it does not suppress the instability completely (Zweibel & Kulsrud 1975; Foglizzo & Tagger 1994, 1995; Matsuzaki et al. 1998; Kowal et al. 2003). However, rotation introduces a fundamentally new feature to the system: under the action of the Coriolis force, the gas flows produced by the instability become helical and can drive mean-field dynamo action that generates a magnetic field at a large scale comparable to that of the initial unstable configuration. Hanasz (1997), Hanasz & Lesch (1997, 1998) and Thelen (2000a) simulate numerically the mean-field dynamo action driven by the magnetic buoyancy with and without cosmic rays, while Moss et al. (1999) present an analytical formulation. A striking feature of the nonlinear evolution of a rotating system, noticed by Machida et al. (2013) in their simulations of the galactic dynamo using ideal magnetohydrodynamics (MHD), is the possibility of quasi-periodic magnetic field reversals at the time scale of 1.5 Gyr, both near the disc midplane and at large altitudes. This appears to be an essentially nonlinear effect that relies on rotation since the linear instability does not develop oscillatory solutions and the nonlinear states are not oscillatory without rotation (Tharakkal et al. 2022a). Foglizzo & Tagger (1994, their Section 7.1) find that the Parker instability can be oscillatory in a certain range of the azimuthal wave numbers. Machida et al. (2013) relate the reversals to the magnetic flux conservation, but we note that the *large-scale* magnetic flux is not conserved when the mean-field dynamo is active. Our simulations of the nonlinear Parker instability in a rotating system suggest a different, more subtle explanation that relies on the correlations between magnetic and velocity fluctuations not dissimilar to those arising from the α-effect that drives the mean-field dynamo action (see below). Large-scale magnetic fields whose horizontal direction alternates with height emerge in the simulations of mean-field dynamo action by Hanasz et al. (2004). This spatial pattern may be related to the field reversals near the midplane.

© 2022 The Authors

Table 1. The list of simulation runs discussed: the numerical resolutions along each axis, the angular velocity and rotational shear, and the instability growth rate computed for u_z and b_z.

	$(\Delta x, \Delta y, \Delta z)$ [pc]	Ω $[\mathrm{km\,s^{-1}\,kpc^{-1}}]$	S $[\mathrm{km\,s^{-1}\,kpc^{-1}}]$	Γ $[\mathrm{Gyr^{-1}}]$
Ω00N	(15,7,13)	0	0	23
Ω30N	(31,15,27)	30	0	22
Ω30S	(31,15,27)	30	−30	12
Ω60S	(31,15,27)	60	−60	7

We explore the effects of rotation on the Parker instability in a numerical model similar to that of Tharakkal et al. (2022a), quantifying both its linear and nonlinear stages and identifying the roles of the Coriolis force and the velocity shear of the differential rotation. We consider the instability in a local rectangular box with parameters similar to those of the Solar neighbourhood of the Milky Way. The structure of this paper is as follows. Section 2 describes briefly the numerical model, and in Section 3 we consider the linear stage of the instability. Section 4 presents a detailed comparison of the distributions of the thermal and non-thermal components of the system in the nonlinear, saturated stage of the instability and how they change when the rotational speed and shear rate vary. in Section 5, we clarify the mechanism of the magnetic field reversal and Section 8 discusses the effects of rotation on the systematic vertical flows. The mean-field dynamo action of the motions induced by the instability is our subject in Section 6 where we discuss the kinetic and magnetic helicities.

2 BASIC EQUATIONS AND THE NUMERICAL MODEL

We use a model very similar to that of Tharakkal et al. (2022a), with the only difference being that we now consider rotating systems, with either a solid-body or differential rotation. We consider the frame rotating at the angular velocity of the centre of the domain with the z-axis aligned with the gravitational acceleration and the angular velocity $\boldsymbol{\Omega}$, the y-axis directed along the azimuth and the x-axis parallel to the radial direction of the local cylindrical frame. Vector x-components are occasionally referred to as radial, while y-components are called azimuthal.

The non-ideal MHD equations are formulated for the gas density ρ, its velocity $\boldsymbol{U}$, total pressure P (which includes the thermal, magnetic and cosmic-ray contributions), magnetic field $\boldsymbol{B}$ and its vector potential $\boldsymbol{A}$, and the energy density of cosmic rays ϵ_{cr}. The initial conditions represent an unstable magneto-hydrostatic equilibrium, and the corresponding distributions ρ_0, $\boldsymbol{B}_0$ and $\epsilon_{\mathrm{cr},0}$ in z are maintained throughout the simulation as a background state. We solve for the deviations from them, denoted ρ' for the density, $\boldsymbol{u}$ for the velocity, P' for the total pressure, $\boldsymbol{b}$ for the magnetic field and $\boldsymbol{a}$ for its vector potential, and ϵ'_{cr} and $\boldsymbol{F}'$ for the cosmic-ray energy density and flux. Cosmic rays are described in the fluid approximation with non-Fickian diffusion, so we have separate equations for their energy density and flux. The governing equations are solved numerically in a rectangular shearing box of the size $4\times4\times3.5\,\mathrm{kpc}^3$ along the x, y and z axes, respectively, with the mid-plane at $z = 0$ and $|z| \leq 1.75\,\mathrm{kpc}$. The boundary conditions are periodic in x, sliding-periodic in y and allow for a free exchange of matter through the top and bottom of the domain as specified in detail by Tharakkal et al. (2022a).

The total velocity is given by $\boldsymbol{U} = \boldsymbol{U}_0 + \boldsymbol{u}$, where $\boldsymbol{U}_0 = Sx\hat{\boldsymbol{y}}$ is the mean rotation velocity in the rotating frame with the shear rate $S = x\,\mathrm{d}\Omega/\mathrm{d}x$, and $\boldsymbol{u}$ is the deviation from this, associated with the instability. For a solid-body rotation, $S = 0$, we have $\boldsymbol{U}_0 = 0$. Both S and Ω are assumed to be independent of z and $S < 0$ for realistic galactic rotation profiles. We neglect the vertical gradient of Ω and S; for its observed magnitude of order -15–$25\,\mathrm{km\,kpc^{-1}}$ (Section 10.2.3 of Shukurov & Subramanian 2021, and references therein), Ω and S only vary by about 10–15 per cent within $|z| \lesssim 1.5\,\mathrm{kpc}$.

The presence of rotation only affects the momentum and induction equations, so equations (1), (4)–(6), (9) and (10) for the mass conservation and cosmic rays of Tharakkal et al. (2022a) still apply and only the momentum and induction equations are augmented with terms containing Ω and S:

$$\frac{\mathrm{D}\boldsymbol{u}}{\mathrm{D}t} = -\frac{\nabla P}{\rho} + \boldsymbol{g} + \frac{(\nabla\times\boldsymbol{B})\times\boldsymbol{B}}{4\pi\rho} - Su_x\hat{\boldsymbol{y}} - 2\boldsymbol{\Omega}\times\boldsymbol{u} + \nabla\cdot\boldsymbol{\tau}\,, \qquad (1)$$

$$\frac{\partial\boldsymbol{a}}{\partial t} = \boldsymbol{u}\times(\nabla\times\boldsymbol{A}) - Sa_y\hat{\boldsymbol{x}} - Sx\frac{\partial\boldsymbol{a}}{\partial y} - \eta\nabla\times(\nabla\times\boldsymbol{a})\,, \qquad (2)$$

where $\mathrm{D}/\mathrm{D}t = \partial/\partial t + (\boldsymbol{U}_0 + \boldsymbol{u})\cdot\nabla$ is the Lagrangian derivative, $\boldsymbol{g}$ is the gravitational acceleration and $\boldsymbol{\tau}$ is the viscous stress tensor. The Kepler gauge for the vector potential, as described by Oishi & Mac Low (2011) (see also Brandenburg et al. 1995), is appropriate for this shearing box framework.

We use the gravity field $\boldsymbol{g} = -g(z)\hat{\boldsymbol{z}}$ obtained by Kuijken & Gilmore (1989) for the Solar vicinity of the Milky Way and consider an isothermal gas with the sound speed $c_{\mathrm{s}} = 18\,\mathrm{km\,s^{-1}}$ and temperature $T = 3.2\times10^4\,\mathrm{K}$. In the background state (identified with the subscript zero, this is also the initial state), both the magnetic and cosmic ray pressures are adopted to be half the thermal pressure, $P_{\mathrm{m},0}/P_{\mathrm{th},0} = P_{\mathrm{cr},0}/P_{\mathrm{th},0} = 0.5$, where $P_{\mathrm{th},0} = c_{\mathrm{s}}^2\rho_0(0)$, $P_{\mathrm{m},0} = B_0^2(0)/(8\pi)$ and $P_{\mathrm{cr},0} = \epsilon_{\mathrm{cr}0}(0)/3$ are the thermal, magnetic and cosmic ray pressures, respectively, and $B_0(0) = 5\,\mathrm{\mu G}$. The gas viscosity ν (included in $\boldsymbol{\tau}$) and magnetic diffusivity η are chosen as $\nu = 0.1\,\mathrm{kpc\,km\,s^{-1}}$ and $\eta = 0.03\,\mathrm{kpc\,km\,s^{-1}}$, respectively, to be somewhat smaller than the turbulent values in the ISM (see Tharakkal et al. 2022a, for further details and justification).

Table 1 presents the simulation runs discussed in this paper. The value of Ω near the Sun is close to $30\,\mathrm{km\,s^{-1}\,kpc^{-1}}$ (referred to as the nominal value hereafter), and $S = -\Omega$ when the rotational speed is independent of the galactocentric distance (a flat rotation curve), $|\boldsymbol{\Omega}\times\boldsymbol{r}| = \mathrm{const}$. Model Ω00N is identical to Model Sim6 of Tharakkal et al. (2022a), Model Ω30N only differs by the solid-body rotation at the nominal angular velocity, Model Ω30S adds the large-scale velocity shear (differential rotation), whereas Model Ω60S has both the angular velocity and its shear doubled. The averages at $z = \mathrm{const}$ (horizontal averages) are denoted $\langle\cdots\rangle_{\mathrm{h}}$.

Figure 1 presents a pictorial summary of the changes in the magnetic field and gas density as the instability develops through its linear stage and then saturates in Model Ω30S. During the linear phase, at $t = 0.3\,\mathrm{Gyr}$, the magnetic field and gas density retain the structure of the imposed fields with weak perturbations in ρ. By the weakly nonlinear stage at $t = 0.6\,\mathrm{Gyr}$, both the gas density and magnetic field are strongly perturbed to the extent that the mean azimuthal magnetic field $\langle B_y\rangle_{\mathrm{h}}$ starts reversing. The reversal is complete in the late nonlinear stage at $t = 1.6\,\mathrm{Gyr}$ and magnetic loops are prominent. We explain and detail these processes below.

3 THE LINEAR INSTABILITY

The linear phase of the Parker instability in the absence of rotation is discussed in detail in our previous work (Tharakkal et al. 2022a), where we compare the growth rate and the spatial structure

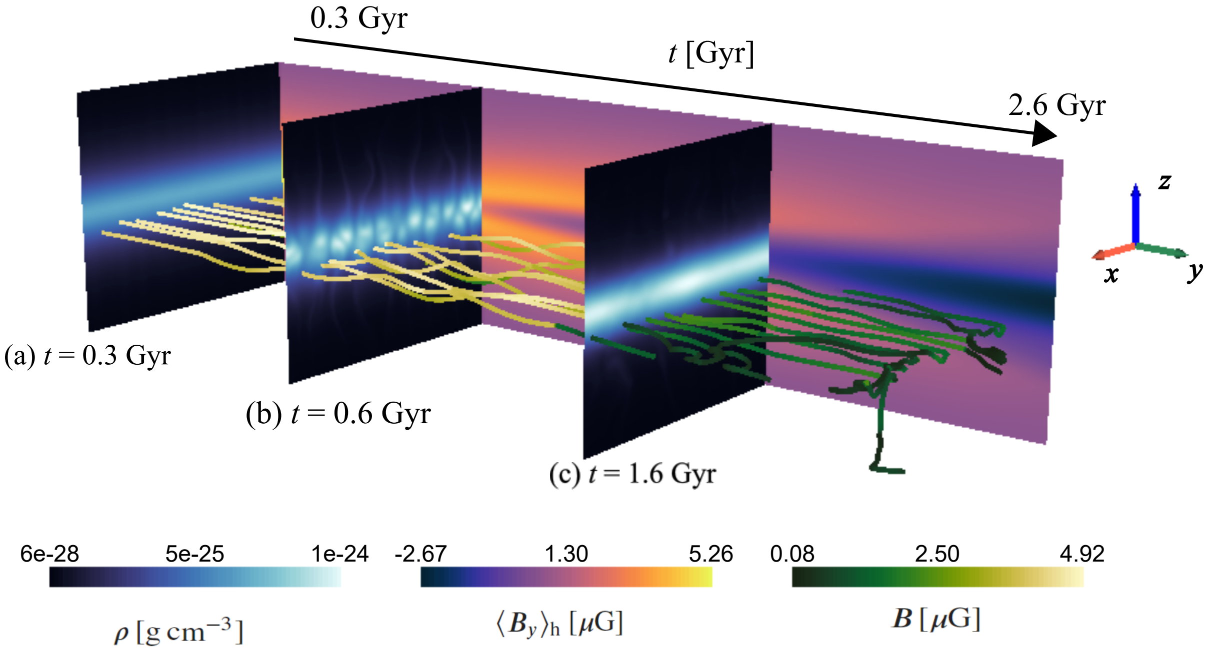

Figure 1. The evolution of the gas density and magnetic field in Model Ω30S is illustrated for its three significant epochs: **(a)** the linear stage, **(b)** beginning of the magnetic field reversal in the early nonlinear stage and **(c)** the advanced nonlinear state (the specific simulation times are indicated for each frame). Selections of magnetic lines are shown (with colour representing the local magnetic field strength in μG) in the (x, y, z)-space at the time indicated to the left of each frame. The horizontal average of the azimuthal magnetic field $\langle B_y \rangle_\mathrm{h}$ in μG is shown with colour on the vertical (z, t)-plane as it evolves continuously (rather than at discrete times used for the magnetic lines). The gas density distribution is shown with colour on the vertical (x, z)-planes (in $\mathrm{g\,cm^{-3}}$) for each time.

of the most rapidly growing mode with those obtained in a range of analytical and numerical models. In this section, we focus on the modifications of the exponentially growing perturbations caused by the rotation and velocity shear.

Figures 2a,b show the evolution (in both the linear and nonlinear stages) of the root-mean-square (r.m.s.) magnitudes of the perturbations in the magnetic field and velocity, while Panels (c) and (d) show how the total magnetic field strength $B_\mathrm{r.m.s.}$ and the mean cosmic ray energy density ϵ_cr at $z = 0$, respectively, evolve in the models of Table 1. As expected (Shu 1974; Zweibel & Kulsrud 1975; Foglizzo & Tagger 1994, 1995; Hanasz & Lesch 1997), the instability growth rate Γ (given in Table 1) decreases systematically with the angular velocity. The stretching of the magnetic lines along the radial (x) direction by the Coriolis force enhances the magnetic tension thus opposing the instability while the differential rotation shears the perturbations to reduce the radial wavelength also suppressing the instability (Foglizzo & Tagger 1994).

The spatial structure of the unstable modes is illustrated in Fig. 3, which presents the two-dimensional power spectra of the perturbations affected by the solid-body (c–d) and differential (e–f) rotation and compares them with the non-rotating case (a–b). The spectra of the velocity and magnetic field perturbations are identical when $\Omega = 0$ but noticeable differences develop in rotating systems. In agreement with the analysis of Shu (1974), the dominant azimuthal wave number k_y decreases under the influence of rotation. The solid-body rotation leads to wider spectra in the radial and azimuthal wave numbers, consistent with the weaker variation of the instability growth rate with k_y in a rotating system (Fig. 1 of Foglizzo & Tagger 1994). Since the Coriolis force couples the radial and azimuthal motions, the spectra in k_x and k_y are more similar to each other than in the case $\Omega = 0$. However, the velocity shear strongly reduces the range of k_y while the perturbations have significantly larger radial wave numbers k_x than in the cases $\Omega = 0$ and $S = 0$.

4 THE SATURATED STATE

Figure 2 also shows that the nonlinear development of the instability and its statistically steady state are strongly affected by the rotation and velocity shear. Solid-body rotation does not affect much the magnitude of the magnetic field perturbations at $t \gtrsim 1$ Gyr, presented with the solid and dash-dotted curves in Panel (a), but reduces the velocity perturbations shown in Panel (b). Understandably, the velocity shear enhances both (the dotted curves) by stretching the radial magnetic fields which, in turn, affect the motions. The case of faster rotation and correspondingly stronger shear confirms this tendency (dashed curves).

Panels (c) and (d) of Fig. 2, which show the total magnetic field strength and cosmic ray energy density at $z = 0$, suggest that the structure of the magnetic field is changed profoundly by rotation and, especially, by the velocity shear. For example, the magnitude of the magnetic field perturbations in Model Ω30S shown with the dotted curve in Panel (a) is less than twice larger than at $\Omega = 0$ (solid curve), but the total magnetic field at $z = 0$ shown in Panel (c) is almost an order of magnitude stronger since the perturbation is better localised near $z = 0$ (see below). The instability still removes both the magnetic field and cosmic rays from the system as in the case $\Omega = 0$, but at a much lower efficiency that depends on both the angular velocity and the rotational shear.

As compared to the case $\Omega = 0$, the system retains stronger magnetic field under the solid-body rotation but less cosmic rays, as shown with the solid and dash-dotted curves in Fig. 2(c,d). Figure 4 clarifies the details of the changes effected by rotation and velocity

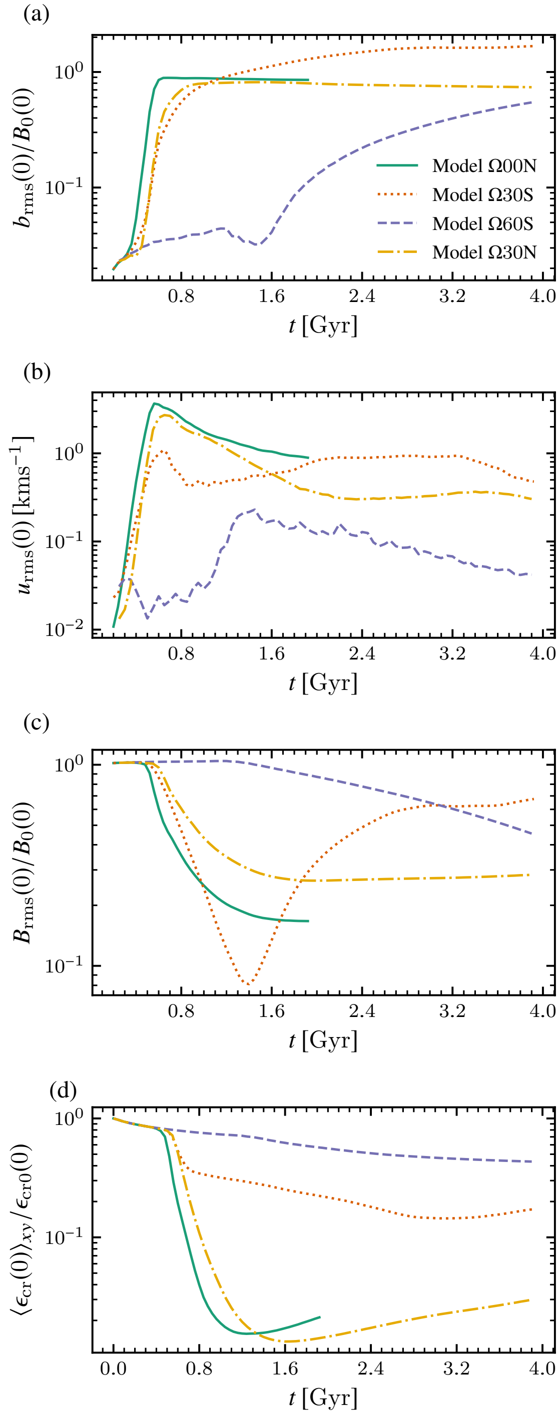

Figure 2. The evolution of the root-mean-square magnitudes at the midplane $z = 0$ of **(a)** the magnetic field perturbation $|\boldsymbol{b}|$, normalised to $B_0(0)$ (the strength of the background magnetic field at $z = 0$), and **(b)** gas speed in the Models Ω00N (solid, no rotation), Ω30N (dash-dotted, solid-body rotation at the nominal Ω), Ω30S (dotted, differential rotation at the nominal Ω and S) and Ω60S (dashed, doubled Ω and S). Similarly, panels **(c)** and **(d)** show the horizontally averaged total magnetic and cosmic ray energy densities at $z = 0$ for those models, normalized to the respective midplane values in the background state, $\langle B\rangle_{xy}(0)/B_0(0)$ and $\langle\epsilon_{\rm cr}\rangle_{xy}(0)/\epsilon_{\rm cr0}(0)$, respectively.

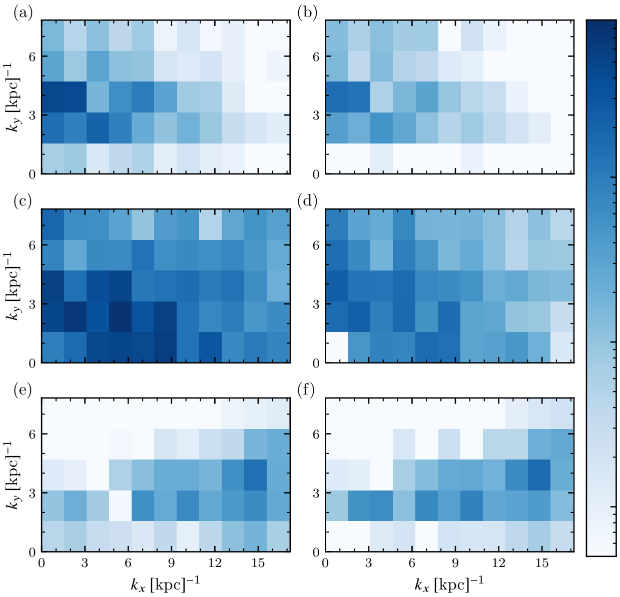

Figure 3. The two-dimensional power spectra of u_z (left column, in the units of kpc^2 km^2 s^{-2}) and b_z (right column, in kpc^2 μG^2), averaged over $|z| < 1.75$ kpc, in Models Ω00N (a–b), Ω30N (c–d) and Ω30S (e–f) at $t = 0.3$ Gyr (the linear stage of the instability).

shear, presenting the varying vertical profiles of the gas density, magnetic fields and cosmic rays in Models Ω00N, Ω30N and Ω30S. Both solid-body and differential rotations reduce the gas scale height in the saturated state. The comparison of Panels (b–c) and (e–f) shows that the solid-body rotation leads to narrower distributions (smaller scale heights) of both magnetic field and cosmic rays about the midplane. Moreover, as we discuss below, the gas flow becomes helical in a rotating system (see Section 6), supporting the mean-field dynamo action. As a result, a large-scale radial magnetic field B_x, clearly visible in Fig. 5(d,f), emerges in a rotating system.

The velocity shear changes the nonlinear state qualitatively. Firstly, the scale heights of B and $\epsilon_{\rm cr}$ near the midplane are even smaller at $t = 0.6$–0.9 Gyr in Panels (h) and (i) than at the comparable times in Panels (e) and (f). Secondly, and more importantly, the vertical profile of the magnetic field strength evolves to become more complicated at $t = 1.6$ Gyr in Panel (h), and the cosmic ray distribution reflects this change. The energy density of cosmic rays in Model Ω30S, $\langle\epsilon_{\rm cr}\rangle_{\rm h}(0) = 0.2\epsilon_{\rm cr0}$ at $t = 1.6$ Gyr (Fig. 4i) is ten time larger than in Model Ω00N. Differential rotation helps to confine cosmic rays because it drives dynamo action generating strong horizontal magnetic field, and this slows down the escape of cosmic rays as they spread along larger distances guided by the magnetic field.

The change in the vertical profile of $\langle B\rangle_{\rm h}$ in Model Ω30S at $t = 1.6$ Gyr reflects the reversal of the horizontal magnetic field near the midplane discussed and explained in Section 5.

5 MAGNETIC FIELD REVERSAL

The reversal of the magnetic field in the nonlinear stage of the instability has been noticed earlier by a few authors (see Section 1) but our simulations identify it as a generic feature of the Parker and magnetic buoyancy instabilities in rotating systems. This process is illustrated in Fig. 5 which shows how the evolution of the large-scale

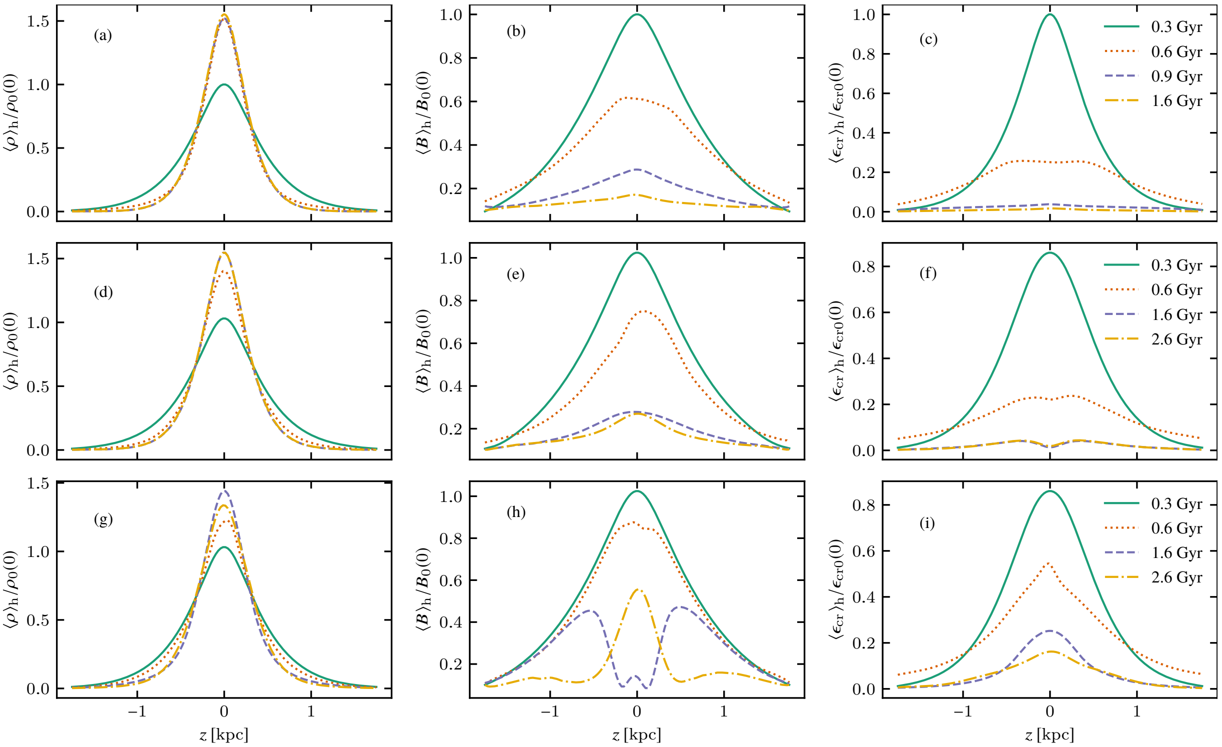

Figure 4. The evolution of the vertical profiles of the horizontally averaged and normalised gas density $\langle\rho\rangle_{\rm h}/\rho_0(0)$ (left-hand column), magnetic field strength $\langle B\rangle_{\rm h}/B_0(0)$ (middle) and cosmic ray energy density $\langle\epsilon_{\rm cr}\rangle_{\rm h}/\epsilon_{\rm cr0}(0)$ (right-hand column). First row: Model Ω00N (no rotation), second row: Model Ω30N (nominal solid-body rotation), third row: Model Ω30S (nominal rotation and shear). The times corresponding to the line styles are given in the legend of each row. Note that the direction of the mean azimuthal magnetic field $\langle B_y\rangle_{\rm h}$ has reversed within a certain distance of the midplane at the later times, $t = 1.6$ and 2.6 Gyr.

horizontal magnetic field components $\langle B_x\rangle_{\rm h}$ and $\langle B_y\rangle_{\rm h}$ depends on rotation and the velocity shear.

Figure 5a shows again (see also Tharakkal et al. 2022a, for details) that, in a non-rotating system, the azimuthal magnetic field $\langle B_y\rangle_{\rm h}$ decreases with time in strength and its scale height increases, while the radial field $\langle B_x\rangle_{\rm h}$ shown in Fig. 5b is much weaker and varies along z without any systematic pattern. Solid-body rotation causes two major changes: the azimuthal field strength (Fig. 5c) first decreases faster than without rotation but then starts growing and, at late times, is stronger than for $\Omega = 0$. The field direction remains the same as of the imposed field, $\langle B_y\rangle_{\rm h} > 0$. Meanwhile, the radial field (Fig. 5d) is, at late times, comparable in strength to $\langle B_y\rangle_{\rm h}$, well-ordered and is predominantly negative, $\langle B_x\rangle_{\rm h} < 0$. This change is a result of the mean-field α^2-dynamo action driven by the mean helicity of the gas flow as discussed in Section 6.

The differential rotation of Model Ω30S (Fig. 5e,f) changes the evolution even more dramatically: it drives the more efficient $\alpha\omega$-dynamo with stronger $\langle B_x\rangle_{\rm h}$ and, remarkably, exhibits a reversal of the large-scale horizontal magnetic field. The reversal starts in the weakly nonlinear phase at $t = 0.5$ Gyr with a rather abrupt emergence of a relatively strong positive radial magnetic field near the midplane, $\langle B_x\rangle_{\rm h} > 0$. The velocity shear with $S < 0$ stretches the positive radial field into a negative azimuthal magnetic field, so that $\langle B_y\rangle_{\rm h}$ starts decreasing and reverses at $t = 1.6$ Gyr (Fig. 5e). The total horizontal magnetic field strength $(\langle B_x\rangle_{\rm h}^2 + \langle B_y\rangle_{\rm h}^2)^{1/2}$ decreases to a minimum before increasing again, as $\langle B_y\rangle_{\rm h}$ decreases to zero and then re-emerges with the opposite direction. These changes in the large-scale magnetic field structure start near the midplane and spread to larger altitudes because of the magnetic buoyancy.

5.1 The mechanism of the reversal

To understand the process that leads to the reversal of the large-scale azimuthal magnetic field, we consider individual terms in the induction equation written for the deviation from the imposed magnetic field,

$$\frac{\partial \boldsymbol{b}}{\partial t} = -(\boldsymbol{U}\cdot\nabla)\boldsymbol{B} + (\boldsymbol{B}\cdot\nabla)\boldsymbol{U} - \boldsymbol{B}\nabla\cdot\boldsymbol{U} + \eta\nabla^2\boldsymbol{b}\,. \qquad (3)$$

Figure 6 shows, for Model Ω30S, the evolution of the mean radial and azimuthal components of the first three terms on the right-hand side of this equation, which represent the advection, stretching and compression of the corresponding magnetic field components near the midplane. The stretching terms $(\boldsymbol{B}\cdot\nabla)U_x$ and $(\boldsymbol{B}\cdot\nabla)U_y$ clearly dominate, producing a mean radial field $\langle B_x\rangle_{\rm h} > 0$ during the weakly nonlinear stage, $0.6 \lesssim t \lesssim 0.8$ Gyr, which decreases only slowly at later times (because of diffusion and buoyancy) while being gradually stretched by the differential rotation $S < 0$ into a negative azimuthal field $\langle B_y\rangle_{\rm h}$, eventually leading to the reversal of the initially positive $\langle B_y\rangle_{\rm h}$. This picture is very different from that for Model Ω00N, where the stretching terms in both components rapidly vanish after a negative excursion during the early nonlinear phase (see Figs 5a,b and 7). Under the solid-body rotation, a positive radial field does emerge near $z = 0$ in the early nonlinear stage but, without the velocity shear, this does not lead to the reversal of the azimuthal field (Fig. 5c,d).

We have analyzed various parts of the averaged stretching term $\langle(\boldsymbol{B}\cdot\nabla)U_x\rangle_{\rm h}$ in the x-component of equation (3) to understand which of them produces a positive radial component of the mean field. We

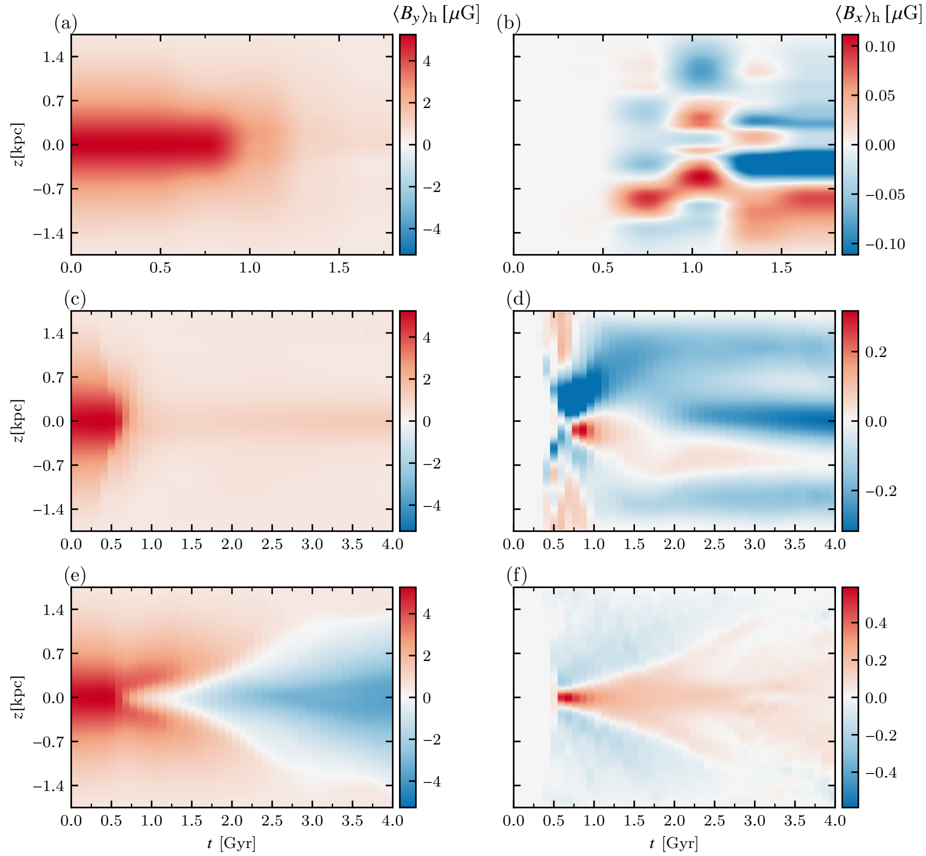

Figure 5. The evolution of the horizontally averaged magnetic field components, $\langle B_y\rangle_\mathrm{h}$ (left-hand column) and $\langle B_x\rangle_\mathrm{h}$ (right-hand column) in Models Ω00N (a–b), Ω30N (c–d) and Ω30S (e–f). For Ω30S the mean azimuthal field $\langle B_y\rangle_\mathrm{h}$ decreases after $t = 0.6$ Gyr, and undergoes a reversal in sign at $t \approx 1.6$ Gyr, with the reversal then spreading to higher altitudes. Meanwhile, the mean radial field $\langle B_x\rangle_\mathrm{h}$ becomes positive and relatively strong near $z = 0$ rather abruptly at $t \approx 0.5$ Gyr and then also spreads away from the midplane.

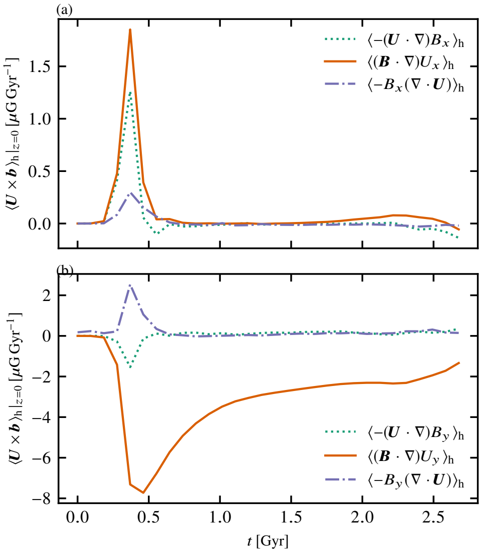

Figure 6. The evolution of the three terms on the right-hand side of the induction equation (3) volume-averaged near the midplane ($z < 0.4$ kpc): **(a)** the radial (x) and **(b)** the azimuthal (y) components of the stretching term $(\boldsymbol{B}\cdot\boldsymbol{\nabla})\boldsymbol{U}$ (solid), advection $-(\boldsymbol{U}\cdot\boldsymbol{\nabla})\boldsymbol{B}$ (dotted) and compression $-B(\boldsymbol{\nabla}\cdot\boldsymbol{U})$ (dash-dotted), in model Ω30S.

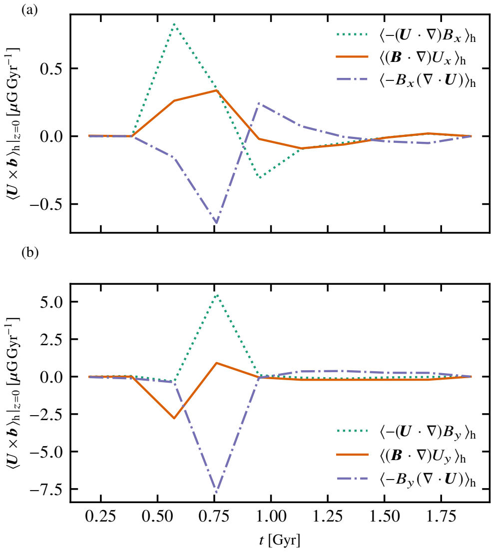

Figure 7. As in Fig. 6, but for model Ω00N.

note that $\langle U_x\rangle_\mathrm{h} = 0$ and then $\langle(\boldsymbol{B}\cdot\nabla)U_x\rangle_\mathrm{h} = \langle(\boldsymbol{b}\cdot\nabla)u_x\rangle_\mathrm{h}$. Thus,

$$\langle(\boldsymbol{B}\cdot\nabla)U_x\rangle_\mathrm{h} = \left\langle b_x\frac{\partial u_x}{\partial x}\right\rangle_\mathrm{h} + \left\langle b_y\frac{\partial u_x}{\partial y}\right\rangle_\mathrm{h} + \left\langle b_z\frac{\partial u_x}{\partial z}\right\rangle_\mathrm{h}. \qquad (4)$$

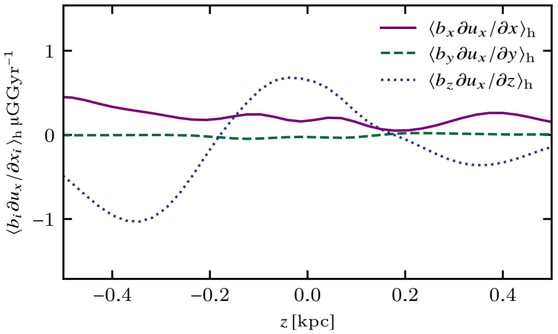

Figure 8. The vertical variation of the horizontally averaged stretching terms in equation (4) in Model Ω30S at $t = 0.7\,$Gyr near the midplane: $\langle b_x\,\partial u_x/\partial x\rangle_\mathrm{h}$ (solid), $\langle b_y\,\partial u_x/\partial y\rangle_\mathrm{h}$ (dashed) and $\langle b_z\,\partial u_x/\partial z\rangle_\mathrm{h}$ (dotted).

Figure 8 shows that the first two terms on the right-hand side of this equation are less significant than the third term, and that $\langle b_z\,\partial u_x/\partial z\rangle_\mathrm{h} > 0$ at $|z| \lesssim 0.2\,$kpc. The term $\langle b_x\,\partial u_x/\partial x\rangle_\mathrm{h}$ also contributes to the generation of a positive $\langle B_x\rangle_\mathrm{h}$ at all z.

The positive correlation between b_z and $\partial u_x/\partial z$, the main driver in the generation of the positive $\langle B_x\rangle_\mathrm{h}$, arises because of: (i) the Coriolis force; and (ii) the emergence of a local minimum of $\langle B_y\rangle_\mathrm{h}$ at the midplane produced by the buoyancy. To demonstrate this, we express u_x using the y-component of the momentum equation (1) with $S = -\Omega$, differentiate the result with respect to z, multiply it by b_z and average to obtain

$$\rho\Omega\left\langle b_z\frac{\partial u_x}{\partial z}\right\rangle_\mathrm{h} = \frac{1}{4\pi}\left\langle b_z^2\frac{\partial^2 B_y}{\partial z^2}\right\rangle_\mathrm{h} + \frac{1}{8\pi}\left\langle\frac{\partial b_z^2}{\partial z}\frac{\partial B_y}{\partial z}\right\rangle_\mathrm{h} + \left\langle b_z\frac{\partial\Psi}{\partial z} - b_z\frac{\partial\rho}{\partial z}\Omega u_x\right\rangle_\mathrm{h}, \qquad (5)$$

where we have neglected the fluctuations in ρ when averaging on the left-hand side (which is justifiable since the random gas speed is subsonic) and Ψ combines all other terms:

$$\Psi = -\rho\frac{\mathrm{D}u_y}{\mathrm{D}t} - \frac{\partial P}{\partial y} - \frac{1}{8\pi}\frac{\partial b^2}{\partial y} + \frac{1}{4\pi}\left(b_x\frac{\partial b_y}{\partial x} + b_y\frac{\partial b_y}{\partial y}\right), \qquad (6)$$

where we neglect the viscosity (represented by the viscous stress tensor $\boldsymbol{\tau}$) and $b^2 = b_x^2 + b_y^2 + b_z^2$. Figures 9a,b show vertical profiles of $\langle B_y\rangle_\mathrm{h}$ in Models Ω30N (where no reversal occurs) and Ω30S, while Fig. 9c clarifies the form of various terms in equation (5). The positive correlation $\langle b_z\,\partial u_x/\partial z\rangle_\mathrm{h}$ emerges because of the first term on the right-hand side as soon as magnetic buoyancy produces a local minimum of $\langle B_y\rangle_\mathrm{h}$ at $z = 0$ (see Fig. 9b), so that $\partial^2 B_y/\partial z^2$ is systematically positive at $z = 0$. Such a minimum does not develop in the case of solid-body rotation (Fig. 9a) where no reversal of $\langle B_y\rangle_\mathrm{h}$ happens. As shown in Fig. 9c, the second and third terms in equation (5) are smaller in magnitude than the first term near $z = 0$ and partially compensate each other. The correlation $\langle b_z\,\partial u_x/\partial z\rangle_\mathrm{h}$ is dominant and positive near $z = 0$, driving a reversal in the large-scale magnetic field near the midplane which then spreads to larger $|z|$ as shown in Fig. 6e,f because of the magnetic buoyancy. We stress that the minimum of $\langle B_y\rangle_\mathrm{h}$ at $z = 0$ can only arise at the nonlinear stage of the instability, because only then do the fluctuations b_y not average to zero.

We have verified that the reversal is not sensitive to the direction of the imposed magnetic field $B_0(z)\hat{\boldsymbol{y}}$; i.e., it occurs in the exactly the same manner for $B_0(z) > 0$ and $B_0(z) < 0$. Our simulations extend to 4 Gyr in duration (see Fig. 5). This is already a significant fraction of the galactic lifetime; therefore, we did not extend them further to find out if a further reversals would occur at later times. However, periodic reversals occur in a similar model where the unstable magnetic field is generated by an imposed *mean-field dynamo action* (Y. Qazi et al. 2022, in preparation). It appears that the emergence of the local minimum of $\langle B_y\rangle_\mathrm{h}$ at $z = 0$ and its ensuing reversal is related to the mean-field dynamo action (which our imposed field emulates). The dynamo is driven by the mean helicity of the gas flow, and both Models Ω30N and Ω30S support this mechanism (as discussed below). However, the dynamo in Model Ω30N, which has solid-body rotation (so is an α^2-dynamo), is too weak, whereas the differential rotation of Model Ω30S enhances the dynamo enough (making it an $\alpha\omega$-dynamo) to produce the reversal. In the next section, we compute and discuss the mean helicity of the gas flow and other evidence for the mean-field dynamo action in Model Ω30S.

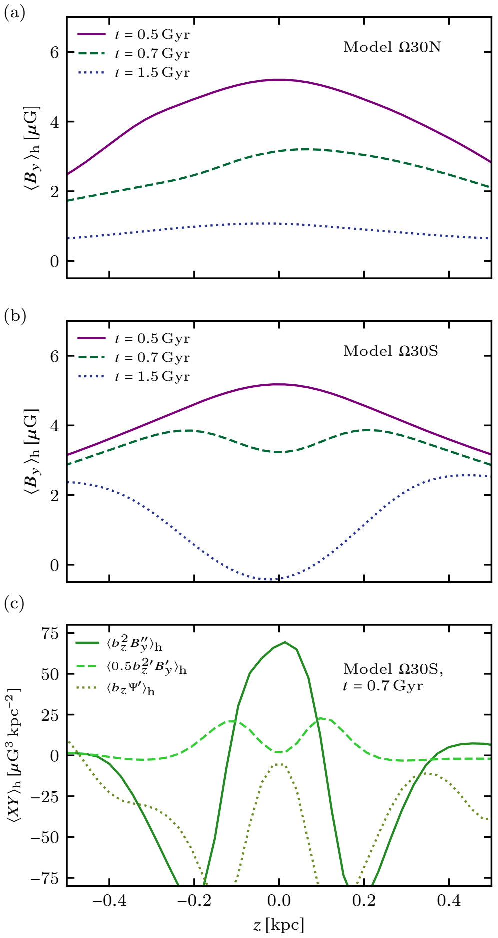

Figure 9. The vertical profiles of the horizontally averaged azimuthal field, $\langle B_y\rangle_\mathrm{h}$, at $= 0.5\,$Gyr (solid), $t = 0.7\,$Gyr (dashed) and $1.5\,$Gyr (dotted) in Models **(a)** Ω30N and **(b)** Ω30S. Panel **(c)** shows the variation with z of the correlations on the right-hand-side of equation (5) for Model Ω30S at $t = 0.7$ Gyr: $\langle (b_z)^2\,\partial^2 B_y/\partial z^2\rangle_\mathrm{h}$ (solid), $\langle \tfrac{1}{2}\partial(b_z)^2/\partial z\,\partial B_y/\partial z\rangle_\mathrm{h}$ (dashed) and $\langle b_z\,\partial\Psi/\partial z\rangle_\mathrm{h}$ (dotted).

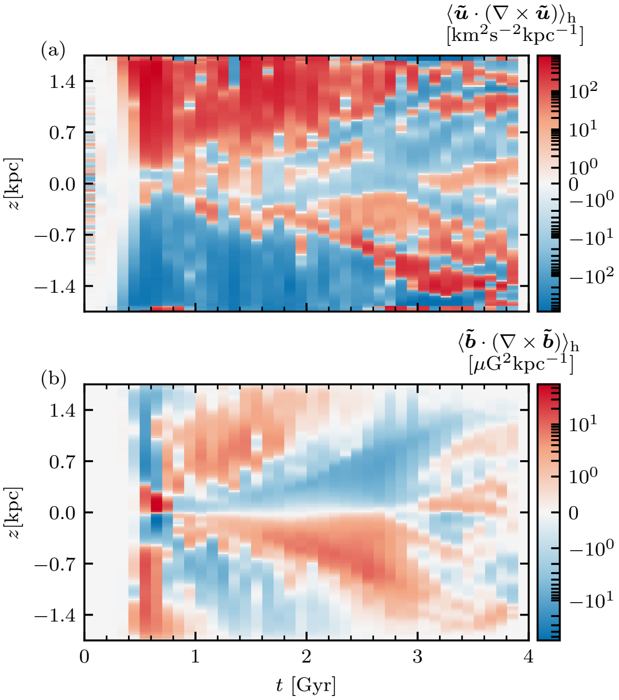

Figure 10. The evolution of the horizontally averaged **(a)** kinetic helicity $\langle\tilde{\boldsymbol{u}}\cdot(\nabla\times\tilde{\boldsymbol{u}})\rangle_{\rm h}$ and **(b)** current helicity $\langle\tilde{\boldsymbol{b}}\cdot(\nabla\times\tilde{\boldsymbol{b}})_{\rm h}\rangle$ in Model Ω30S.

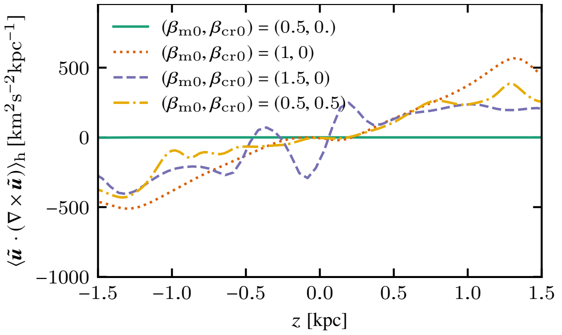

Figure 11. The spatial distribution of the mean kinetic helicity $\chi_{\rm k}$ at $t = 0.7\,$Gyr for four imposed (initial) magnetic field strengths specified by the parameters $\beta_{\rm m,0}$ and $\beta_{\rm cr,0}$ defined in equation (12) and given in the legend. Among the models shown in this figure, cosmic rays are present only in Model Ω30S where $(\beta_{\rm m,0}, \beta_{\rm cr,0}) = (0.5, 0.5)$ (dash-dotted: this is a vertical cross-section of the distribution in Fig. 10a).

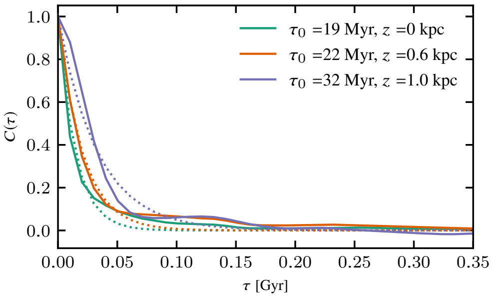

Figure 12. The time autocorrelation function of the vertical velocity component, equation (11), for $0 \le t \le 2\,$Gyr (with the minimum time lag of 10 Myr) at $z = 0$ (solid), 0.6 (dashed) and 1 kpc (dotted) in Model Ω30S. The correlation time τ_0 at each z is given in the legend, obtained from the fits of the form $C(\tau) = \exp(-\tau/\tau_0)$, shown with dotted curves.

6 HELICITY AND DYNAMO ACTION

In Models Ω30N, Ω30S and Ω60S, the Coriolis force causes the gas motions to become helical, and the resulting α-effect produces a large-scale radial magnetic field $\langle B_x\rangle_{\rm h}$ (e.g., Sect. 7.1 of Shukurov & Subramanian 2021). Differential rotation (in Models Ω30S and Ω60S) enhances the dynamo significantly, and we have discovered that this leads to a reversal in the azimuthal magnetic field direction discussed in Section 5. Both types of the turbulent dynamo (α^2 dynamo in Ω30N and $\alpha\omega$ in Ω30S and Ω60S) are driven by the mean kinetic helicity of the gas flow $\chi_{\rm k} = \overline{\tilde{\boldsymbol{u}}\cdot(\nabla\times\tilde{\boldsymbol{u}})}$, and the current helicity of the magnetic fluctuations $\chi_{\rm m} = \overline{\tilde{\boldsymbol{b}}\cdot(\nabla\times\tilde{\boldsymbol{b}})}$ opposes the dynamo instability leading to a reduction of the α-coefficient until a steady state is achieved (e.g., Sect. 7.11 of Shukurov & Subramanian 2021). Here overbar denotes a suitable averaging, and we use the horizontal averages in our discussion, so $\tilde{\boldsymbol{u}}$ and $\tilde{\boldsymbol{b}}$ are understood as the deviations from the horizontal averages $\langle\boldsymbol{B}\rangle_{\rm h}$ and $\langle\boldsymbol{U}\rangle_{\rm h}$, such that

$$\boldsymbol{B} = \langle\boldsymbol{B}\rangle_{\rm h} + \tilde{\boldsymbol{b}}\,, \quad \boldsymbol{U} = \langle\boldsymbol{U}\rangle_{\rm h} + \tilde{\boldsymbol{u}}\,, \quad \left\langle\tilde{\boldsymbol{b}}\right\rangle_{\rm h} = 0\,, \quad \langle\tilde{\boldsymbol{u}}\rangle_{\rm h} = 0\,. \tag{7}$$

Figure 10 shows the evolution of the kinetic and current helicities and their variation with z obtained using the horizontal averages. As expected, both quantities have odd symmetry in z (e.g., Sect. 11.3.1 of Shukurov & Subramanian 2021). Both are weak throughout the linear phase when the instability-driven perturbations are still weak, but increase significantly in magnitude during the early nonlinear phase at about $t = 0.5\,$Gyr. The kinetic helicity reaches its maximum magnitude $|\chi_{\rm k}| = |\langle\tilde{\boldsymbol{u}}\cdot(\nabla\times\tilde{\boldsymbol{u}}\rangle_{\rm h}| = 851\,\mathrm{km^2\,s^{-2}\,kpc^{-1}}$ near the upper and lower boundaries, $z = \pm1.6\,$kpc, during the transitional phase at $t = 0.6\,$Gyr. At a later time, $t = 1.9\,$Gyr, the kinetic helicity reduces to a maximum of $|\chi_{\rm k}| = 340\,\mathrm{km^2\,s^{-2}\,kpc^{-1}}$ at $|z| = 1.6\,$kpc. At early stages of the evolution, the current helicity has local extrema close to the midplane, where the magnetic field is stronger, $|\chi_{\rm m}| = |\langle\tilde{\boldsymbol{b}}\cdot(\nabla\times\tilde{\boldsymbol{b}})\rangle_{\rm h}| = 89\,\mu\mathrm{G^2\,kpc^{-1}}$ at $t = 0.6\,$Gyr, $|z| = 0.1\,$kpc. The extrema move away from the midplane in the nonlinear stage, to reach $|\chi_{\rm m}| = 7\,\mu\mathrm{G^2\,kpc^{-1}}$ at $t = 1.2\,$Gyr, $|z| = 0.5\,$kpc and $|\chi_{\rm m}| = 5\,\mu\mathrm{G^2\,kpc^{-1}}$ at $t = 3\,$Gyr, $|z| = 1\,$kpc.

The vertical profiles of both kinetic and current helicities evolve in a rather complicated manner, with $\chi_{\rm k} < 0$ at $z > 0$ close to the midplane (although the magnitude is small), and $\chi_{\rm k} > 0$ at larger z in the case of pure magnetic buoyancy (dotted curve in Fig. 11 representing $t = 0.7\,$Gyr). In Model Ω30S, $\chi_{\rm k} < 0$ at $z > 0$ close to the midplane just before $t = 0.7\,$Gyr. Negative $\chi_{\rm k}$ at $z > 0$ is expected from the action of the Coriolis force on the ascending and descending volume elements (Sect. 7.1 of Shukurov & Subramanian 2021). However, $\chi_{\rm k} > 0$, as it occurs at larger z for all models presented in Fig. 11, is unexpected (see below for a discussion).

The α-coefficient of the nonlinear mean-field dynamo is related to the kinetic and current helicities as (Sect. 7.11.2 of Shukurov & Subramanian 2021)

$$\alpha = \alpha_{\rm k} + \alpha_{\rm m}\,, \tag{8}$$

where, in terms of the horizontal averages,

$$\alpha_{\rm k} = -\tfrac{1}{3}\tau_0\langle\tilde{\boldsymbol{u}}\cdot(\nabla\times\tilde{\boldsymbol{u}})\rangle_{\rm h}\,, \qquad \alpha_{\rm m} = \tfrac{1}{3}\tau_0\frac{\langle\tilde{\boldsymbol{b}}\cdot(\nabla\times\tilde{\boldsymbol{b}})\rangle_{\rm h}}{4\pi\rho}\,, \tag{9}$$

and τ_0 is the characteristic (correlation) time of the random flow.

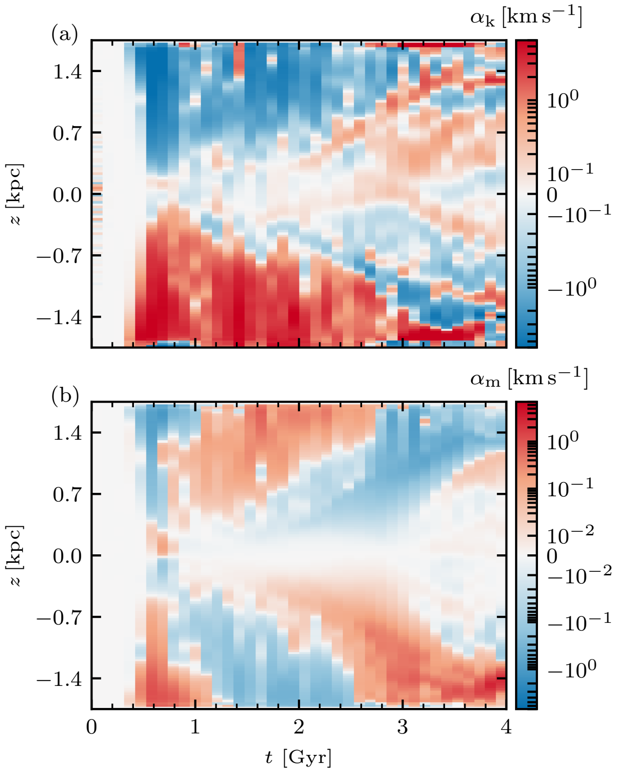

Figure 13. The evolution of **(a)** $\alpha_{\rm k}$ and **(b)** $\alpha_{\rm m}$, given in equations (9), in Model Ω30S.

The relevant time scale τ_0 differs from the time scale of the linear instability $2\pi/(u_0 k_y)$ where u_0 and k_y are the characteristic speed and azimuthal wave number of the most unstable mode shown in Figs 2b and Fig. 3e–f, respectively. Instead, τ_0 is determined by nonlinear effects and has to be measured separately. We calculate the correlation time using the time autocorrelation function $C(\tau)$ of u_z (the vertical velocity u_z is a representative component since it is directly related to the instability),

$$\tau_0 = \int_0^\infty C(\tau)\,{\rm d}\tau\,, \tag{10}$$

with the normalized autocorrelation function calculated as

$$C(\tau) = \frac{1}{T\,\langle \tilde{u}_z^2\rangle_{\rm h}} \left\langle \int_0^T \tilde{u}_z(t,\boldsymbol{x})\tilde{u}_z(t+\tau,\boldsymbol{x})\,{\rm d}t \right\rangle_{\rm h}\,, \tag{11}$$

where T is the duration of the time series used to compute $C(\tau)$. For a given z, the integral in equation (11) is calculated for each (x, y) and the result is averaged over (x, y). Thus defined, the autocorrelation function and the corresponding correlation time depend on z.

Figure 12 shows the time autocorrelation of u_z at three values of z, and the form $C(\tau) = \exp(-\tau/\tau_0)$ provides a good fit, with the fitted values of τ_0 given in the legend: they vary between 18 Myr at $z = 0$ and 40 Myr at $z = 1.5$ kpc. We use the fitted $C(\tau)$ to estimate τ_0 as this provides a more accurate result than the direct integration as in the definition (10).

We use $\tau_0 = 30$ Myr in equations (9), and the results are shown in Fig. 13. The largest in magnitude values $|\alpha_{\rm k}| \approx 7\,{\rm km\,s^{-1}}$ are reached during the transition phase around $t = 0.6$ Gyr near $|z| = 1.5$ kpc, whereas $|\alpha_{\rm m}|$ is at its maximum around $3\,{\rm km\,s^{-1}}$ during the nonlinear phase at $t = 3.6$ Gyr.

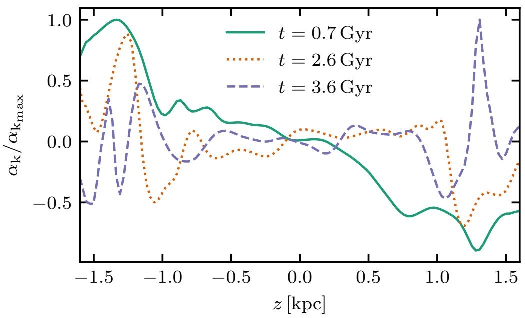

Figure 14. The variation of the normalised $\alpha_{\rm k}$ with z in the early ($t = 0.7$ Gyr, solid) and late ($t = 2.6$ Gyr, dotted, $t = 3.6$ Gyr, dashed) nonlinear stages in Model Ω30S.

The spatial structure of $\alpha_{\rm k}$ is relatively simple during the early nonlinear phase but becomes more complicated later. Closer to the midplane and at later stages of the evolution, $\alpha_{\rm k} > 0$ at $z > 0$ (and $\alpha_{\rm k} < 0$ at $z < 0$) as expected, and the region where $\alpha_{\rm k}$ is predominantly positive (albeit small in magnitude) extends to larger $|z|$ with time (see Fig. 14 representing vertical sections of Fig. 13a).

As expected, the sign of the current helicity is opposite to that of $\alpha_{\rm k}$ at almost all z and t, so that the back-reaction of the magnetic field on the flow weakens the dynamo action leading to a (statistically) steady state at $t \gtrsim 3$ Gyr.

The negative sign of $\alpha_{\rm k}$ at $z > 0$ (corresponding to the positive kinetic helicity $\chi_{\rm k}$) appears to be a specific feature of a system driven by magnetic buoyancy or another magnetically driven instability such as the magneto-rotational instability (MRI). Hanasz & Lesch (1998) argue, using a model of reconnecting magnetic flux ropes, that negative $\alpha_{\rm k}$ at $z > 0$ can occur in magnetic buoyancy-driven mean-field dynamos. In his analysis of the mean electromotive force produced by the magnetic buoyancy instability in its linear stage, Thelen (2000a, his Fig. 4) finds $\alpha < 0$ in the unstable region of the northern hemisphere in spherical geometry (corresponding to $z > 0$ in our case), although the 'anomalous' sign of $\alpha_{\rm k}$ remained unnoticed (Thelen 2000b). However, Brandenburg & Schmitt (1998) find $\alpha_{\rm k} > 0$ at $z > 0$ in their analysis of the α-effect due to magnetic buoyancy. Brandenburg & Sokoloff (2002) find $\alpha_{\rm k} < 0$ at $z > 0$ in simulations of the MRI-driven dynamos (their Section 2 and α_{yy} in Figs 5, 7, 9 and 11). Kinetic helicity (and the corresponding $\alpha_{\rm k}$) of this 'anomalous' sign is also found in the simulations of MRI-driven dynamos of P. Dhang et al. (2023, in preparation) (K. Subramanian 2022, private communication). The origin and properties of the kinetic helicity of random flows driven by magnetic buoyancy and MRI deserves further attention. Our results indicate not only that the kinetic helicity has the anomalous sign but also that it can change in space and time.

The current helicity (Fig. 10b) and the corresponding contribution to the α-effect (Fig. 13b) have the opposite signs to, and closely follow both the spatial distribution and evolution of, $\chi_{\rm k}$ and $\alpha_{\rm k}$ respectively (although the magnetic quantities have smoother spatial distributions than the corresponding kinetic ones). This confirms that the action of the Lorentz force on the flow weakens the dynamo action as expressed by equation (8). Together with the removal of the large-scale magnetic field by the Parker instability, this leads to the eventual evolution of the system to the statistically steady state.

Although the gas flows that become helical are driven by the instability, no simple and obvious relation of the mean helicity to the parameters that control the strength of the instability is apparent. Figure 11 shows how the vertical profile of the kinetic helicity $\chi_{\rm k}$

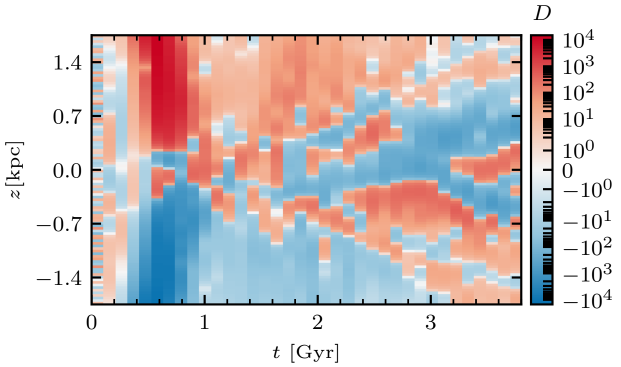

Figure 15. The evolution and vertical variation of the dynamo number of equation (13) in Model Ω30S.

changes with the magnetic and cosmic ray pressures in the initial (imposed) state, specified in terms of their ratios to the thermal pressure at $z = 0$,

$$\beta_{\rm m0} = \frac{B_0(0)^2}{8\pi c_{\rm s}^2 \rho_0(0)} \quad \text{and} \quad \beta_{\rm cr0} = \frac{(\gamma_{\rm cr} - 1)\epsilon_{\rm cr0}(0)}{c_{\rm s}^2 \rho_0(0)}\,, \tag{12}$$

where $\gamma_{\rm cr} = 4/3$. To avoid complications associated with the cosmic rays in the system behaviour, only one model of the four illustrated in Fig. 11 contains cosmic rays (Model Ω30S discussed elsewhere in the text). The midplane strengths of the imposed magnetic field $B_0(0)$ corresponding to $\beta_{\rm m0} = 0.5, 1$ and 1.5 are 5, 7 and 9 μG, respectively. When $(\beta_{\rm m0}, \beta_{\rm cr0}) = (0.5, 0)$, the magnetic field is too weak to be unstable and the system remains in the state of magneto-hydrostatic equilibrium, $\chi_{\rm k} = 0$. Adding cosmic rays, $(\beta_{\rm m0}, \beta_{\rm cr0}) = (0.5, 0.5)$ (Model Ω30S) destabilises the system producing helical flows discussed above. Adding magnetic rather than cosmic ray pressure, $(\beta_{\rm m0}, \beta_{\rm cr0}) = (1, 0)$, also makes the system unstable, and the resulting mean helicity at larger $|z|$ is greater than for $(\beta_{\rm m0}, \beta_{\rm cr0}) = (0.5, 0.5)$. A still stronger magnetic field, $(\beta_{\rm m0}, \beta_{\rm cr0}) = (1.5, 0)$ leads to comparable $\chi_{\rm k}$ the previous two cases in $|z| \lesssim 1$ kpc, except near the midplane. Altogether, it is difficult to identify a clear pattern in the dependence of the magnitude and spatial distribution of the mean helicity of the gas flow driven by the Parker instability; this invites further analysis, both analytical and numerical.

The dimensionless measure of the mean-field dynamo activity in a differentially rotating gas layer is provided by the dynamo number (Section 11.2 of Shukurov & Subramanian 2021)

$$D = \frac{\alpha S h^3}{\beta^2}\,, \tag{13}$$

where h is the layer scale height, S is the velocity shear rate ($S = -\Omega$ in our case), α is given in equation (8) and

$$\beta = \tfrac{1}{3}\tau_0 \langle \tilde{u}^2 \rangle_{\rm h} + \eta \tag{14}$$

is the magnetic diffusivity. The first term in this expression is the turbulent diffusivity and η is the explicit magnetic diffusivity from equation (2) or (3). As we use the horizontal averages in these relations, D is a function of z and varies with time together with h, α and β; thus defined, D might be better called the local dynamo number, a measure of the dynamo efficiency at a given z and t. In Model Ω30S, $\eta = 0.03\,{\rm kpc\,km\,s^{-1}}$ while the turbulent diffusivity varies, at $t = 1$ Gyr, from $0.03\,{\rm kpc\,km\,s^{-1}}$ at $z = 0$ to $0.5\,{\rm kpc\,km\,s^{-1}}$ at $z = 1$ kpc (a nominal turbulent diffusivity in the ISM, where turbulence is mainly driven by supernovae, is $1\,{\rm kpc\,km\,s^{-1}}$). The dynamo amplifies a large-scale magnetic field provided $|D| > D_{\rm c}$, where $D_{\rm c}$ is a certain critical dynamo number (see below).

Table 2. The cross-correlation coefficient r of the fluctuations in various energy densities in the statistically steady state of Model Ω30S at $t = 2.6$ Gyr presented as a, b, where a and b refer to $z = 0.5$ and 1 kpc, respectively.

	$\epsilon'_{\rm th}$	$\epsilon'_{\rm cr}$	$\epsilon'_{\rm m}$	$\epsilon'_{\rm k}$
$\epsilon'_{\rm th}$	1, 1	0.2, −0.03	−0.02, −0.2	−0.14, 0.12
$\epsilon'_{\rm cr}$		1, 1	−0.4, −0.8	0.2, 0.05
$\epsilon'_{\rm m}$			1,1	−0.29, −0.1
$\epsilon'_{\rm k}$				1, 1

Figure 15 shows how the dynamo number varies with t and z. During the transient phase, $\langle \tilde{u}^2 \rangle_{\rm h}$ is relatively low while $|\alpha|$ is at its maximum. The resulting dynamo number is as large as $|D| \simeq 10^4$. As the system evolves into the nonlinear state, the turbulent diffusivity increases and the dynamo number reduces in magnitude. At $t = 0.6$ Gyr, D varies from 4 near the midplane to 6×10^3 at $z = 1$ kpc. At later times, D is larger near the midplane and reduces further in magnitude: at $t = 0.9$ Gyr, $D = 300$ near the midplane and 9 at $z = 1$ kpc.

As shown by Ruzmaikin et al. (1980), the $\alpha\omega$-dynamo in flat geometry generates oscillatory magnetic fields for $D > 0$, quadrupolar for $D \gtrsim 180$ and dipolar for $D \gtrsim 550$. The behaviour of the large-scale magnetic field in Model Ω30S is consistent with these results: it is quadrupolar and oscillatory.

7 RELATIVE DISTRIBUTIONS OF COSMIC RAYS AND MAGNETIC FIELD

Similar to our analysis in Tharakkal et al. (2022a), we present in Table 2 the Pearson cross-correlation coefficient between the fluctuations in energy densities for different components in model Ω30S at $z = 0.5$ and 1 kpc for the late nonlinear stage at $t = 2.6$ Gyr, derived as

$$\begin{aligned} \epsilon'_{\rm m} &= \frac{B^2 - \left\langle B^2 \right\rangle_{\rm h}}{8\pi}\,, \qquad \epsilon'_{\rm cr} = \epsilon_{\rm cr} - \langle \epsilon_{\rm cr} \rangle_{\rm h}\,, \\ \epsilon'_{\rm th} &= c_{\rm s}^2 \left(\rho - \langle \rho \rangle_{\rm h}\right), \qquad \epsilon'_{\rm k} = \tfrac{1}{2}\rho\tilde{u}^2 - \left\langle \tfrac{1}{2}\rho\tilde{u}^2 \right\rangle_{\rm h}\,. \end{aligned} \tag{15}$$

The only significant entry in the table is the anti-correlation between the magnetic and cosmic ray energy fluctuations at $z = 1$ kpc where their contribution to the total pressure is noticeable (see Section 8). There are no signs of energy equipartition between cosmic rays and magnetic fields at kiloparsec scales; nor are there indications of equipartition at the turbulent scales, for either cosmic ray protons (Seta et al. 2018) or electrons (Tharakkal et al. 2022b).

8 VERTICAL FLOWS AND FORCE BALANCE

Rotation affects significantly the vertical gas flow driven by the instability. As discussed by Tharakkal et al. (2022a) (and also in Model Ω00N), a systematic gas outflow is transient without rotation and only occurs during the early nonlinear stage. Figure 16 shows the horizontally averaged vertical velocity $\langle u_z \rangle_{\rm h}$ in Models Ω30N (solid-body rotation) and Ω30S (differential rotation). In both cases, systematic vertical flows occur at $|z| \gtrsim 1$ kpc. The solid-body rotation (Fig. 16a) does not change much the structure of the flow in

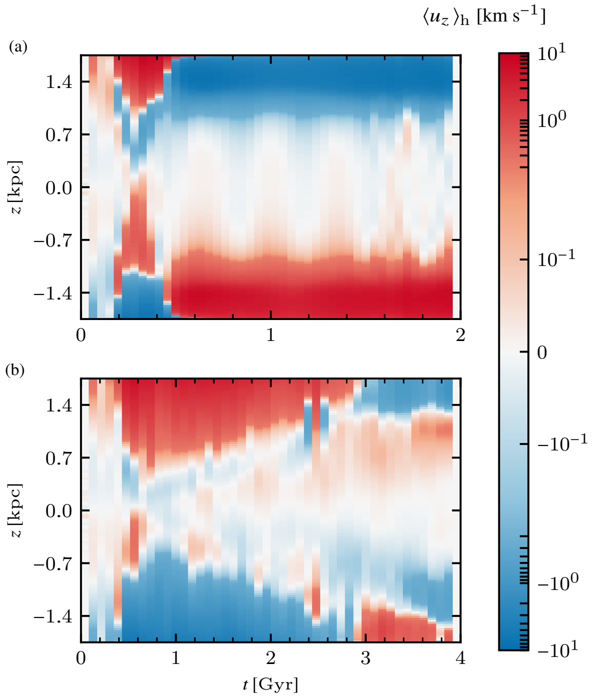

Figure 16. The evolution and variation with z of the horizontally averaged vertical velocity $\langle u_z \rangle_\mathrm{h}$ in Models **(a)** Ω30N and **(b)** Ω30S.

comparison with the non-rotating system, with a transient outflow during the early nonlinear stage and a weak inflow at later times. In Model Ω30N, the maximum outflow speed is $|\langle u_z \rangle_\mathrm{h}| = 9\,\mathrm{km\,s^{-1}}$ at $t = 0.7\,\mathrm{Gyr}$, followed by the inflow at the speed $|\langle u_z \rangle_\mathrm{h}| = 7\,\mathrm{km\,s^{-1}}$ at $t > 1.4\,\mathrm{Gyr}$. However, differential rotation not only changes dramatically the magnetic field structure and evolution (Fig. 5), but also supports a prolonged period of a systematic gas outflow at $0.6 \lesssim t \lesssim 3\,\mathrm{Gyr}$, which eventually evolves into a weak gas inflow at large $|z|$ (Fig. 16b). The maximum outflow speed in Model Ω30S is $|\langle u_z \rangle_\mathrm{h}| = 7\,\mathrm{km\,s^{-1}}$ at $t = 0.6\,\mathrm{Gyr}$ at large $|z|$, while the later inflow speed is $|\langle u_z \rangle_\mathrm{h}| = 1\,\mathrm{km\,s^{-1}}$ at $t \gtrsim 3\,\mathrm{Gyr}$.

The pattern of the vertical flows shown in Fig. 16b is not dissimilar to the structure of the magnetic field shown in Fig. 5e–f and the dynamo number (Fig. 15) — especially at later stages, $t \gtrsim 3\,\mathrm{Gyr}$ — suggesting that the magnetic field contributes noticeably to the vertical flow in Model Ω30S.

To understand what drives the vertical flows, we present in Fig. 17 the vertical forces acting during various evolutionary stages of Model Ω30S. It is instructive to compare them with those in non-rotating systems discussed by Tharakkal et al. (2022a). Without rotation, as in Model Ω00N (see also Fig. 12 of Tharakkal et al. 2022a), both magnetic and cosmic ray pressures are reduced significantly as the system evolves into the nonlinear state, and the vertical gas flows are driven by the thermal pressure gradient. This changes in Model Ω30S, where magnetic field, and to a lesser extent cosmic rays, make a stronger contribution to the force balance. Moreover, the gravity force and the thermal pressure gradient balance each other almost completely in the nonlinear state, so that the weaker magnetic and cosmic ray pressures appear to be capable of controlling the vertical velocity pattern, especially at $|z| \gtrsim 0.5\,\mathrm{kpc}$. This is is illustrated in Fig. 18, which shows that the vertical variations of the net vertical force per unit mass are indeed similar in detail to those of the magnetic pressure gradient.

The magnetic and cosmic ray pressure gradients are weak because both non-thermal components of the simulated ISM are much less stratified than the thermal gas. However, their energy densities are large and they dominate over the thermal gas at $|z| \gtrsim 0.5$–$1\,\mathrm{kpc}$. Figure 19 shows the vertical profiles of the horizontally averaged ratios of the magnetic and cosmic ray pressures to the thermal pressure, β_m and β_cr respectively, defined as in equation (12) but for the evolving quantities. Although each non-thermal pressure component is subdominant near the midplane at all stages of the evolution, each of them exceeds the thermal pressure at larger altitudes as soon as the instability becomes nonlinear, $t \gtrsim 0.6\,\mathrm{Gyr}$. It is useful to compare Fig. 19 with Fig. 18 of Tharakkal et al. (2022a): rotation somewhat reduces the magnitudes of β_m and β_cr at large $|z|$ but leads to the dominance of the non-thermal pressure components at smaller values of $|z|$ than in a non-rotating system, and leads to a larger contribution from cosmic rays.

9 DISCUSSION AND CONCLUSIONS

Differential rotation affects the nonlinear state of the Parker instability more strongly than its linear properties. Without rotation, the system loses most of its magnetic field and cosmic rays as it evolves towards the steady state. A solid-body rotation does not change the nonlinear state significantly. However, differential rotation allows the system to retain better both the magnetic field and cosmic rays. The reason for that is the dynamo action (present also under the solid-body rotation but significantly enhanced by the differential rotation) which produces strong (about 2–3 μG) large-scale magnetic field both near the midplane and at large altitudes. As a result, cosmic rays (governed by anisotropic diffusion) spend longer times within the system.

The systematic vertical gas flows are also affected by the rotation, which prolongs the transient outflow at a speed $|\langle u_z \rangle_\mathrm{h}| = 7\,\mathrm{km\,s^{-1}}$ to the time interval $0.6 \lesssim t \lesssim 3\,\mathrm{Gyr}$. It appears that the magnetic field contributes significantly to driving the outflow. Meanwhile, cosmic rays do not play any significant role in driving the outflow at the scales explored here, $|z| \leq 1.5\,\mathrm{kpc}$: because of the large diffusivity of cosmic rays, the vertical gradient of their pressure is very small.

Another dramatic effect of the dynamo action is that it leads to a reversal of the large-scale magnetic field, in what appears to be a sign of nonlinear oscillations of the large-scale magnetic field. Neither the Parker instability nor the dynamo are oscillatory by themselves. We have identified the rather subtle mechanism of the reversal and argue that it is an essentially nonlinear phenomenon.

The reversal of the large-scale magnetic field is also reflected in its spatial distribution. The reversal starts near the midplane and then the reversed magnetic field spreads to larger altitudes (see Fig. 5e–f). As a result, the direction of the large-scale magnetic field reverses along z at any given time. An arguably similar pattern of regions with the sign of the Faraday depth alternating along the direction perpendicular to the disc plane is observed in the edge-on galaxy NGC 4631 (Mora-Partiarroyo et al. 2019). The comparison of Figs 5e–f and 5c–d shows that the Parker instability in a dynamo active system can produce rather complicated magnetic field structures. Our use of horizontal averages in Fig. 5 and elsewhere in the text conceals strong localised vertical magnetic fields typical of the magnetic buoyancy (see, e.g., Fig. 1), also observed in NGC 4631. Because of the low gas density at kpc-scale distances from the galactic midplane, observations of the Faraday rotation produced there are difficult; the observations of Mora-Partiarroyo et al. (2019) are the first of this kind, and future observation should show how widespread are such complex patterns. Further observational and theoretical studies of large-scale magnetic fields outside the discs of spiral galaxies promise new, unexpected

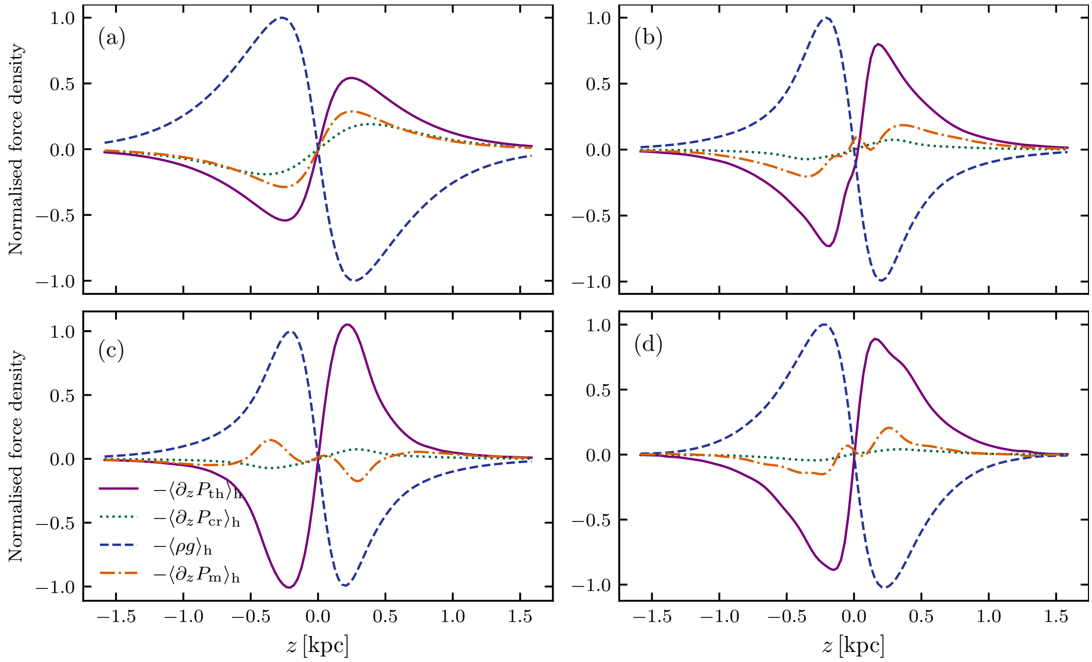

Figure 17. The vertical profiles of the horizontally averaged vertical forces in Model Ω30S normalised to the maximum magnitude of the gravitational force (dashed, repeated in all panels for reference): thermal (solid), cosmic ray (dotted) and magnetic (dash-dotted) pressure gradients. The contribution of the magnetic tension is much weaker, so it is not shown. Each panel represents a different evolutionary stage: **(a)** $t = 0.3$ Gyr (linear instability), **(b)** 0.6 Gyr (transitional); **(c)** 1.6 Gyr (nonlinear state when the magnetic field has just reversed near $z = 0$) and **(d)** 3.6 Gyr (late nonlinear stage).

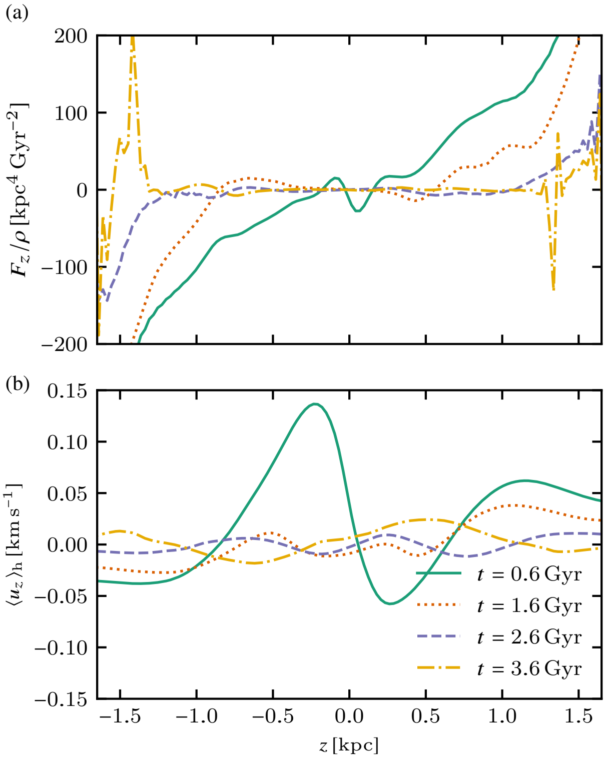

Figure 18. **(a)** The total vertical force per unit mass and **(b)** the resulting vertical velocity at times $t = 0.6$ (solid), 1.6 (dotted), 2.6 (dashed) and 3.6 Gyr (dash-dotted).

insights into the dynamics of the interstellar gas and its magnetic fields.

An unusual feature of our results, which needs further effort to be understood, is that the mean kinetic helicity of the flows driven by the Parker and magnetic buoyancy instabilities is positive in the upper half-space, $z > 0$, and thus has the sign opposite to that in conventional stratified, rotating, non-magnetised systems. We note that positive kinetic helicity also occurs in some earlier studies of the mean-field dynamo action and α-effect in magnetically-driven systems. However, this remarkable circumstance, which can have profound — and poorly understood — consequences for our understanding of the nature of large-scale magnetic fields outside galactic discs, has attracted relatively little attention.

ACKNOWLEDGEMENTS

We are grateful to Axel Brandenburg and Kandaswamy Subramanian for useful discussions. G.R.S. would like to thank the Isaac Newton Institute for Mathematical Sciences, Cambridge, for support and hospitality during the programme 'Frontiers in dynamo theory: from the Earth to the stars', where work on this paper was undertaken. This work was supported by EPSRC grant no. EP/R014604/1.

DATA AVAILABILITY

The raw data for this work were obtained from numerical simulations using the open-source PENCIL-CODE available at `https://github.com/pencil-code/pencil-code.git`). The derived data used for the analysis are available on request from Devika Tharakkal.

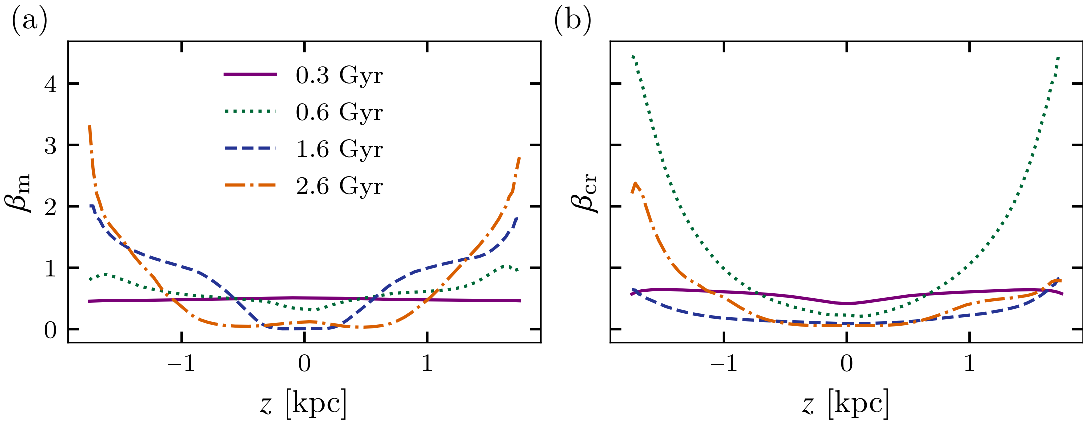

Figure 19. The distribution in z of the horizontally averaged ratios of **(a)** magnetic and **(b)** cosmic ray pressures to the thermal pressure in Model Ω30S, β_m and β_cr, respectively, at various times specified in the legend: the linear state, $t = 0.3$ Gyr (solid), transitional period, $t = 0.6$ Gyr (dotted), nonlinear state at $t = 1.6$ Gyr when the magnetic field reversal occurs (dashed) and a late nonlinear state, $t = 2.6$ Gyr (dash-dotted).

REFERENCES

Brandenburg A., Schmitt D., 1998, A&A, 338, L55
Brandenburg A., Sokoloff D., 2002, Geophys. Astrophys. Fluid Dyn., 96, 319
Brandenburg A., Nordlund A., Stein R. F., Torkelsson U., 1995, ApJ, 446, 741
Foglizzo T., Tagger M., 1994, A&A, 287, 297
Foglizzo T., Tagger M., 1995, A&A, 301, 293
Hanasz M., 1997, A&A, 327, 813
Hanasz M., Lesch H., 1997, A&A, 321, 1007
Hanasz M., Lesch H., 1998, A&A, 332, 77
Hanasz M., Kowal G., Otmianowska-Mazur K., Lesch H., 2004, ApJ, 605, L33
Kowal G., Hanasz M., Otmianowska-Mazur K., 2003, A&A, 404, 533
Kuijken K., Gilmore G., 1989, MNRAS, 239, 571
Machida M., Nakamura K. E., Kudoh T., Akahori T., Sofue Y., Matsumoto R., 2013, ApJ, 764, 81
Matsuzaki T., Matsumoto R., Tajima T., Shibata K., 1998, in Watanabe T., Kosugi T., Sterling A. C., eds, Observational Plasma Astrophysics: Five Years of Yohkoh and Beyond. Springer Netherlands, Dordrecht, pp 321–324, doi:10.1007/978-94-011-5220-4_52
Mora-Partiarroyo S. C., et al., 2019, A&A, 632, A11
Moss D., Shukurov A., Sokoloff D., 1999, A&A, 343, 120
Oishi J. S., Mac Low M.-M., 2011, ApJ, 740, 17
Ruzmaikin A. A., Sokoloff D. D., Turchaninov V. L., 1980, Soviet Ast., 24, 182
Seta A., Shukurov A., Wood T. S., Bushby P. J., Snodin A. P., 2018, MNRAS, 473, 4544
Shu F. H., 1974, A&A, 33, 55
Shukurov A., Subramanian K., 2021, Astrophysical Magnetic Fields: From Galaxies to the Early Universe. Cambridge University Press, Cambridge, doi:10.1017/9781139046657
Tharakkal D., Snodin A. P., Sarson G. R., Shukurov A., 2022b, arXiv:2205.01986, pp 1–19
Tharakkal D., Shukurov A., Gent F. A., Sarson G. R., Snodin A. P., Rodrigues L. F. S., 2022a, arXiv:2212.03215, pp 1–18
Thelen J. C., 2000a, MNRAS, 315, 155
Thelen J. C., 2000b, MNRAS, 315, 165
Zweibel E. G., Kulsrud R. M., 1975, ApJ, 201, 63

This paper has been typeset from a TEX/LATEX file prepared by the author.